Published in final edited form as:
Sci Transl Med. 2016 November 23; 8(366): 366ra165. doi:10.1126/scitranslmed.aaf2593.

A Soft, Wearable Microfluidic Device for the Capture, Storage, and Colorimetric Sensing of Sweat

Ahyeon Koh[1,†], **Daeshik Kang**[1,2,†], **Yeguang Xue**[3], **Seungmin Lee**[1], **Rafal M. Pielak**[4], **Jeonghyun Kim**[1,5], **Taehwan Hwang**[1], **Seunghwan Min**[1], **Anthony Banks**[1], **Philippe Bastien**[6], **Megan C. Manco**[7], **Liang Wang**[3,8], **Kaitlyn R. Ammann**[9], **Kyung-In Jang**[1], **Phillip Won**[1], **Seungyong Han**[1], **Roozbeh Ghaffari**[10], **Ungyu Paik**[5], **Marvin J. Slepian**[9], **Guive Balooch**[4], **Yonggang Huang**[3], and **John A. Rogers**[1,*]

---

[*] Corresponding Author. jrogers@illinois.edu.
[†] Contributed equally to this work

Competing interests: The authors declare no competing financial interests. John Rogers, Ahyeon Koh, Daeshik Kang, YuHao Liu, and Xian Huang are inventors on PCT Patent Application PCT/US2015/044638 submitted by The Board of Trustees of the University of Illinois that covers "Devices and Related Methods for Epidermal Characterization of Biofluids."

Data and materials availability: All data needed to evaluate the conclusions are present in the paper and/or in the Supplementary Materials. Additional data related to this paper may be requested from the authors.

Supplementary Materials
http://stm.sciencemag.org/content/suppl/2016/11/21/8.366.366ra165.DC1
Materials and Methods
Fig. S1. Fabrication procedures of the epidermal microfluidic device using soft lithography
Fig. S2. Determination of adhesion forces and conformal adhesion between the device and skin.
Fig. S3. Observations of sweat at the interface between an adhesive layer and the skin.
Fig. S4. Normal (A) and shear (B) stress distribution at the device/skin interface under 30% stretch plotted on deformed skin.
Fig. S5. Mechanical modeling results for NFC electronics.
Fig. S6. Color balancing performed by internal calibration makers (black crosses and white circle) under various light conditions (A-F) and changes in numeric RGB representation obtained by respective images (G) before and (H) after white balance.
Fig. S7. Image processing for position calibration. (A) Original image and magnified images (B) before and (C) after position calibration
Fig S8. Cross sectional sketch of the microfluidic channel and outlet channel geometry used, and analytical analysis of backpressure and inner pressure.
Fig. S9. Strategies and optimization of the orbicular channel design.
Fig. S10. Schematic illustration of the artificial sweat pore system.
Fig. S11. Hydrodynamic test to verify the influence of the hydrogel matrix on channel volume.
Fig. S12. Assessment of the angular position of the liquid front in partially filled serpentine channels in devices with different hydrogel concentrations and segmented hydrogel patterns.
Fig. S13. Quantitative colorimetric analysis of glucose detection at low concentrations.
Fig. S14. Colorimetric analysis of device response as a function of time after introduction of artificial sweat.
Fig. S15. Various device configurations.
Fig. S16. Multivariate statistical analysis for correlations in biomarker concentrations between patch (p) and lab (l) analysis.
Movie S1. Near field communication between an epidermal microfluidic device and a smart phone to launch software for image capture and analysis.
Movie S2. Near field communication between an epidermal microfluidic device and a smart phone to launch software for temperature sensing.
Movie S3. Hydrodynamic flow in the serpentine channel of epidermal microfluidics on the artificial pore system
Movie S4. Hydrodynamic flow in the detection reservoir of epidermal microfluidics on the artificial pore system
References (57, 58)

Author contributions: D.K., A.K., and J.A.R. led the development of the concepts, designed the experiments, interpreted results, and wrote the paper. D.K. and A.K. led the experimental works, with support from S.L., R.M.P., J.K., T.H., S.M., A.B., P.B., M.C.M., K.R.A., K.-I.J., P.W., R.G., and S.H.. Y.X., L.W., and Y.H. performed mechanical modeling and simulations. S.L. contributed to the image analysis, and R.M.P., P.B., M.C.M., K.R.A., M.J.S., and G.B. contributed to the organization and design of the human test and provided in depth discussion. R.M.P., P.B., and G.B. performed statistical analysis. M.J.S., R.M.P., Y.H, and J.A.R. provided technical guidance. All authors contributed to proofreading the manuscript.

[1]Department of Materials Science and Engineering, Frederick Seitz Materials Research Laboratory, University of Illinois at Urbana-Champaign, Urbana, IL 61801, USA

[2]Department of Mechanical Engineering, Ajou University, Suwon, 443-749, Korea

[3]Departments of Civil and Environmental Engineering, Mechanical Engineering, and Materials Science and Engineering, Northwestern University, Evanston, IL 60208, USA

[4]L'Oréal Technology Incubator, San Francisco, California 94107, USA

[5]Department of Energy Engineering, Hanyang University, Seoul, 133-791, Republic of Korea

[6]L'Oréal Research and Innovation, Aulnay-sous-Bois, France

[7]L'Oréal Early Clinical, Clark, NJ 07066, USA

[8]Department of Chemical and Biological Engineering, Institute of Chemical Machinery and Process Equipment, Zhejiang University, Hangzhou 310027, People's Republic of China

[9]Department of Medicine and Biomedical Engineering, Sarver Heart Center, University of Arizona, Tucson, AZ 85724, USA

[10]MC10 Inc., Cambridge, MA 02140, USA

Abstract

Capabilities in health monitoring via capture and quantitative chemical analysis of sweat could complement, or potentially obviate the need for, approaches based on sporadic assessment of blood samples. Established sweat monitoring technologies use simple fabric swatches and are limited to basic analysis in controlled laboratory or hospital settings. We present a collection of materials and device designs for soft, flexible and stretchable microfluidic systems, including embodiments that integrate wireless communication electronics, which can intimately and robustly bond to the surface of skin without chemical and mechanical irritation. This integration defines access points for a small set of sweat glands such that perspiration spontaneously initiates routing of sweat through a microfluidic network and set of reservoirs. Embedded chemical analyses respond in colorimetric fashion to markers such as chloride and hydronium ions, glucose and lactate. Wireless interfaces to digital image capture hardware serve as a means for quantitation. Human studies demonstrated the functionality of this microfluidic device during fitness cycling in a controlled environment and during long-distance bicycle racing in arid, outdoor conditions. The results include quantitative values for sweat rate, total sweat loss, pH and concentration of both chloride and lactate.

Introduction

A convergence of advances in materials, mechanics design, and specialized device architectures is beginning to establish the foundations for a next generation of wearable electronic technologies, where sensors and other functional components reside not in conventional rigid packages mounted on straps or bands but instead directly on the skin (1, 2). Specifically, devices that combine soft, low-modulus physical properties and thin layouts allow robust, nonirritating, and long-lived interfaces with the human epidermis (2). This developing field involves innovative ideas in both organic and inorganic functional materials, where mechanical and manufacturing science play important roles. Although most devices described in the literature focus on measurement of physical characteristics such as motion, strain, stiffness, temperature, thermal conductivity, biopotential, electrical impedance, and related parameters (1, 3–10), complementary information—often with high clinical value—could be realized through capture and biochemical analysis of biofluids such as sweat (11, 12).

As a representative biofluid, sweat is of particular interest owing to its relative ease of non-invasive collection and its rich content of important biomarkers including electrolytes, small molecules, and proteins (13, 14). Despite the importance of sweat analysis in biomedicine, interpreting information from sweat can be difficult due to uncertainties in its relationship with other biofluids, such as interstitial fluid and blood, and due to the lack of biomedical appliances for direct sampling and detection of multiple biomarkers without evaporation (15). In situ quantitative analysis of sweat is nevertheless of great interest for monitoring of physiologic health status (for example, hydration state) and for the diagnosis of disease (for example, cystic fibrosis) (16, 17). Existing systems for whole-body sweat collection have been confined to the laboratory (18), where standard chemical analysis technologies (chromatography, mass spectroscopy, and electrochemical detection) can reveal the composition of collected samples (19). Recent attempts to detect and collect sweat simultaneously involve direct contact of sensors on the skin (for example, temporary tattoo) where fabric or paper substrates to accumulate sweat for electrochemical and/or optical assessment (20). For instance, electrochemical sensors directly laminated on the epidermis can detect chemical components, such as sodium ions and lactate, in real-time (21–23). Colorimetric responses in functionalized porous substrates can yield chemical information, such as the pH of sweat, and further enable simple quantitative assays using devices capable of capturing high-quality digital images, such as smartphones (24–26). Radio frequency identification systems, which can be integrated on top of porous materials for wireless information transfer, provide additional functionality (27, 28). These and related technologies can quantify sweat generation rate (27), but because the sweat gland density and overall areas are typically unknown, the total sweat rate and volumetric loss cannot be determined accurately. In addition, the most widely explored formats do not simultaneously reveal the concentration of multiple chemical components, nor do they offer full compatibility with the growing availability of soft, skin-mounted electronics, physical sensors, radio technologies, and energy storage devices.

Here, we report a type of thin and soft, closed microfluidic system that can directly and reliably harvest sweat from pores on the surface of the skin. The device routes this sweat to different channels and reservoirs for multiparametric sensing of markers of interest, with options for wireless interfaces to external devices for image capture and analysis. This type of microfluidic technology builds substantially on recently described epidermal electronic, photonic, and optoelectronic systems (1, 29–31) through the addition of fluid handling and capture, and biochemical analytical capabilities. The devices can mount at multiple locations on the body without chemical or physical irritation by use of biocompatible adhesives and soft device mechanics, including flexible and stretchable properties, and watertight interfaces. These devices were able to measure total sweat loss, pH, lactate, chloride, and glucose concentrations by colorimetric detection using wireless data transmission. Tests included two human trials: a controlled, indoor, mild sweat-inducing study, and a "real-world," outdoor-use study conducted during a long distance bicycling race.

RESULTS

Soft epidermal microfluidic device for sweat monitoring

The soft, epidermal microfluidic device technology introduced here adheres and conforms to the skin in a manner that captures and routes sweat through a network of microchannels and reservoirs—using a combination of capillarity and action of the natural pressure (~70 kPa) associated with perspiration—for volumetric assessment and chemical analysis in situ (13). Low-modulus biocompatible materials, soft silicone elastomers (~1 MPa), manipulated using soft lithography defined the microfluidic constructs (diameter, 3 cm; thickness, ~700 μm) (Fig 1 and fig. S1). The specific designs described can retain ~50 μL of sweat corresponding to an effective working time of 1 to 6 hours of exercise, depending on the rate of sweat loss and the mounting location on the body (12 to 120 μL/hour per cm^2) (32). Stretchable electronics technology allows direct integration of wireless sensing and data transfer capabilities into these platforms.

Devices are composed of a multilayer stack of three subsystems: (i) a skin-compatible adhesive layer with micromachined openings that define the areas of sweat collection, (ii) a sealed collection of soft microfluidic channels and reservoirs filled with color-responsive materials for quantitative analysis of sweat volume and chemistry, and (iii) a magnetic loop antenna and associated near-field communication (NFC) electronics for interfacing to external wireless devices (Fig. 1A). A medical-grade acrylic adhesive film ensured stable, strong and seamless adhesion (~5.7 N) of the device to the skin without irritation in a manner that offered compatibility with skin, even at regions of substantial hair coverage or in the presence of sweat (fig. S2). This adhesive exhibited about 5 times greater adhesion force than typical medical adhesives such as Tegaderm (1.02 N) (33). The thin geometry (25 μm) and low modulus (~17 kPa) of this layer provided stress release during deformation of the skin (fig. S2), facilitating comfort and long-term wearability. Openings defined the sweat harvesting areas (3 mm diameter, corresponding to ~10 sweat glands) (34) through which sweat could pass into the inlet regions of the overlying soft microfluidic system (Fig. 1B). The pressure that drives fluid flow arises from the action of the sweat glands themselves, assisted by capillary effects in the microchannels and the materials embedded within them. The conformal contact of the adhesive layer inhibited lateral flow of sweat from regions located outside the defined openings, ensuring fluid issuing from the harvesting area dominated the sweat sample (fig. S3).

The microfluidic system consisted of a bottom polydimethylsiloxane (PDMS) layer (thickness, 500 μm) embossed with appropriate relief geometry (uniform depth, 300 μm) and filled with reagents for colorimetric analysis (Fig. 1, A and B). A top-capping layer of PDMS served as a seal (thickness, 200 μm). Our particular layout included four circular chambers (diameter, 4 mm) as independent reservoirs for analysis, preventing any cross-talk, that were surrounded by the outer perimeter by an orbicular serpentine channel. This channel and each of the reservoirs were connected by separate guiding channels to hole segments (diameter, 0.5 mm) that spatially aligned with the openings (diameter, 3 mm) in the skin adhesive layer (Fig. 1, B and C). To avoid backpressure that can impede fluid flow, all channels and reservoirs interfaced to an outlet microfluidic channel (width, 100 μm) that terminated on the top-side edge of the device (Fig. 1B). Quantitative colorimetric assay reagents in the reservoirs enabled assessment of pH and the concentration of selected essential markers, including glucose, lactate, and chloride, through either enzymatic or chromogenic reactions. Hence, the colorimetric schemes embedded in the current devices did not afford real-time tracking of changes in analyte concentration. A water-responsive chromogenic reagent in the serpentine channel allowed determination of the extent of filling with sweat, which could be converted to overall sweat rate and volume.

Specially formulated variants of PDMS offer physical characteristics that are attractive for this application, including optical transparency, ease of patterning into microfluidic systems, biocompatibility, and favorable mechanics (low modulus, ~145 kPa; high elasticity, up to ~200% strain at break) (35). The soft mechanics and thin geometry enabled soft, nonirritating intimate contact with the skin through principles similar to those established for epidermal electronics (2, 36). The finite element analysis (FEA) results of strain/stress distributions and corresponding optical images in Fig. 1E show deformation of a representative device under various mechanical distortions of an underlying phantom skin sample as a support (a PDMS substrate exhibiting similar mechanical properties to skin). The maximum normal and shear stresses at the device/phantom skin interface were far below the threshold for somatosensory perception of forces (20 kPa) during ~30% stretch of the skin (fig. S4) (37). These elastomeric microfluidic devices exhibited an effective modulus of ~0.16 MPa, comparable to human skin and previously reported epidermal devices (37, 38).

Integrated electronics allow wireless interfaces to external computing and digital analysis systems using common platforms such as the smartphone. Our technology capitalized on NFC schemes to launch image capture and analysis software on such an external device and/or to read temperature from an integrated sensor (movies S1 and S2). The overall designs allowed these stretchable electronic systems to operate under physical deformation without significantly altering the mechanical properties of the soft microfluidic structures or the overall device. FEA results demonstrated that the maximum strain in the copper layer was below the elastic limit (0.3%) under all loading conditions (fig. S5) (39). Reference marks on the top of the device platform (Fig. 1B) included a white dot and black crosses for color balancing to allow accurate color extraction under arbitrary lighting condition (fig. S6). The crosses also helped determine the position and orientation from the images (fig. S7).

Optimizing the design of the epidermal microfluidic device

We optimized materials and channel designs to collect sweat in situ, with soft, stretchable mechanics for high structural stability, low vapor permeability, and minimal backpressure (flow impedance into the channel). Figure 2A is a sketch of the channel geometry, representing the area of the outlet and the serpentine channel, used for theoretical calculation of the essential mechanics and flow properties. The blue and red dashed boxes highlight the dimensions of the serpentine and outlet channels, respectively. The outlet channels are necessary to relieve backpressure, but they also yield some sweat loss as water (sweat) vapor. The water vapor loss showed little dependence on the length of the outlet channel, whereas backpressure was linearly proportional to this length according to calculations for a model system (fig. S8 and Fig. 2B). A short outlet channel length of 2.5 mm was chosen to minimize backpressure. Our calculations further indicated that the vapor loss with 100-μm-wide channels was ~3.2-fold lower than with 800-μm-wide channels, while 25-μm-wide channels differed by only ~1.1-fold from 100-μm-wide channels (Fig. 2B). For widths under 100 μm, the backpressure notably increased and bending deformation of the device was obstructed, with negligible effects on vapor loss. Considering calculated values and practical resolution limits of soft lithography, optimized outlet channel dimensions of 100 μm in width and 2.5 mm in length were selected.

As with vapor loss and backpressure, stretchability and structural stability are two other competing issues that demand careful optimization. Although thin geometries and low-modulus elastomers are key to achieving mechanical compatibility with the skin, such characteristics also yield substantial deformation or even collapse of channels by external pressure (40), either in the as-fabricated form or in states associated with natural deformations of the skin. Modeling yielded predictions for percentage changes in the volume of the serpentine channel associated with externally applied pressures between 100 and 400 Pa (Fig. 2C) comparable to those that might be associated with a gentle touch by a fingertip (41). The volume change increased with the aspect ratio (AR; width to height). For example, the volume change for AR 5 (width, 1.5 mm; height, 300 μm) was about fivefold greater than that for AR 3.3 (width, 1.0 mm; height, 300 μm). Because choices for channel geometries must also consider the total volume of sweat that can be captured and the overall size of the device, we selected the lower limit of AR 3.3. In addition, the serpentine channel layouts provided a convenient means to increase the total channel volume for a given device size (fig. S9). These considerations defined the overall design, the cross-sectional channel dimensions, and the outlet shapes illustrated in Fig. 2D.

Microfluidic sweat capture and quantitative colorimetric analysis

Quantitative *in vitro* testing of microfluidic performance involved a simple, artificial sweat pore system (Fig. 2, E and F, and fig. S10) to mimic human eccrine sweat glands (42), consisting of a perforated PI membrane (pores with diameter 60 μm, ~100 pores per cm^2) mounted in a fixture with an underlying fluid reservoir connected to a syringe pump. A device (0.07 cm^2 of harvesting surface area) laminated on the perforated membrane captured dyed water pumped at 5.5 μl/hour (Fig. 2G), demonstrating the first step in quantitative analysis of liquid uptake (movie S3). As shown in movie S3, the experimentally determined harvested liquid volume in the channel is consistent with the input volume introduced by the syringe pump and with linear hydrodynamic flow in the microfluidic channel. The experiments revealed negligible loss of water vapor and no fluid leakage under these conditions.

Regarding device design, three factors determine the resolution in determination of sweat rate: (i) the rate of fluid flow into the reservoirs and the serpentine channel, (ii) the harvesting area, and (iii) the time and spatial resolution of the camera system and image analysis software. For a device layout with harvesting area (~10 mm^2), the human studies presented subsequently showed volumetric sweat harvesting rates of ~1.2 to 12 μl/hour, corresponding to linear filling rates of ~0.07 to 0.7 mm/min along the serpentine channels. The reservoirs fill within ~0.3 to 3.2 hours at these sweating rates, with times that scale linearly with reservoir volume. Decreasing the cross-sectional area of the channel increases the filling rate proportionally. For image capture once every 5 min, a spatial resolution of ~0.35 to 3.5 mm can easily resolve changes in the positions of the fluid fronts, providing 12 data points within a ~60-min timeframe (13).

The colorimetric sensing approach allowed simple, rapid quantitative assessment of instantaneous rate and total volume of sweat loss, the pH, as well as the concentration of chloride, lactate, and glucose in the sweat (Fig. 3A). The first parameters relate to thermal regulation and dehydration, where continuous monitoring yields important information of relevance to electrolyte balance and rehydration (43). In the orbicular serpentine channel, cobalt (II) chloride (that is, $CoCl_2$) contained in a coating of a polyhydroxyethylmethacrylate (pHEMA) hydrogel matrix served as a colorimetric indicator. As sweat entered the channel, the anhydrous cobalt (II) chloride chelated with water to form hexahydrate cobalt chloride ($CoCl_2{\bullet}6H_2O$), generating a change in color from deep blue (λ_{max} = 657) to pale purple (λ_{max} = 511) (Fig. 3B). The position of the leading edge that defines this color change, along with the dimensional characteristics and geometry of the channel, yields quantitative information on the sweat rate and volume. Owing to the thin layer (~25 μm) coated on the channel wall and the hydrophilic properties of the pHEMA hydrogel matrix, the hydrodynamics of flow within the channel were not influenced during conditions of momentary flow (fig. S11, A to D). The sweat could, however, continue to travel slowly through the channel by spontaneous internal flow (0.68 μl/hour), with the possibility of a ~2% reading error (fig. S11, E and F). This artifact does not occur in channels without the hydrogel; its effect could be eliminated, for practical purposes, by patterning the hydrogel into short segments (fig. S12).

Four different paper-based colorimetric chemical assays resided in the central reservoirs. The cellulose matrices in each reservoir could be filled with as little as 5 to 10 μl of sweat sample. The color changes occurred on timescales of <1 min (movie S4). The concentration of lactate in sweat is an indicator of exercise intolerance and tissue hypoxia (44, 45). Enzymatic reactions between lactate and co-factor NAD^+ (nicotinamide adenine dinucleotide) by lactate dehydrogenase and diaphorase induce a change in color of a chromogenic reagent (that is, formazan dyes). The formulation of enzyme and dyes in the detection cocktail solution ensured a dynamic range compatible with human sweat. The color change in the detection reservoir correlated with the concentration of lactate throughout the relevant range expected in sweat (1.5 to 100 mM) (Fig. 3C) (13, 46, 47).

Glucose concentration could also be analyzed by an enzymatic reaction (Fig. 3D). Glucose oxidase physically immobilized in a cellulose matrix produces hydrogen peroxide associated with oxidation of glucose and reduction of oxygen. After this reaction, iodide oxidizes to iodine by peroxidase, to yield a change in color from yellow (iodide) to brown (iodine), to an extent defined by the concentration of glucose (48, 49). We note that glucose concentration in sweat is typically one order of magnitude lower than in plasma; the range of sensitivity in the reported devices could diagnose hyperglycemia, for example, limit of detection (LOD) = ~200 μM (fig. S13) (50). Further development of colorimetric chemistries based on enzymatic reactions and/or enzyme-mimetic nanomaterials could improve the LODs (51, 52). Similarly, creatinine, a vital marker of hydration status and renal function, was detected in sweat using a mixture of enzymes (creatininase, creatinase, and peroxidase) and a corresponding responsive dye (4-aminophenazone) (Fig. 3E) (53).

In sweat, pH is often considered an index of hydration state. The concentration of chloride ions serves as a marker of cystic fibrosis and altered electrolyte levels correspond to a sodium ion imbalance (17). A universal pH indicator that includes dyes such as bromothymol blue, methyl red, and phenolphthalein yielded colorimetric responses over a medically relevant range (pH 5.0 to 7.0) (Fig. 3F). Colorimetric detection of chloride involved competitive binding between Hg^{2+} and Fe^{2+} with 2,4,6-tris(2-pyridiyl)-s-triazine (TPTZ). In the presence of chloride ions, iron ions (Fe^{2+}) bind with TPTZ, whereas Hg^{2+} participates as $HgCl_2$, thereby inducing a change in color from transparent to blue as shown in Fig. 3G. Although PDMS is known to have some permeability to water and certain small molecules, the colorimetric responses in these devices are unaffected for most practical applications due to the relevant operational timescale and the analyte chemistries used (Fig. S14).

NFC interface to a smartphone and image processing

Recording color changes and converting them into quantitative information were accomplished by digital image capture and analysis. Figure 4A shows frames from a video clip (movie S1) in which the proximity of a smartphone to the device initiated image capture and analysis software automatically using NFC. The user then adjusted the viewing position to the targeted spot to determine exact RGB (red, green, and blue) color in situ. The application digitized RGB color information on the screen, enabling the user to read the concentration of the marker. The previously reported ultrathin NFC electronics (39) integrated on the top of the microfluidic device enabled wireless communication to external devices, with stable operation and a soft, biocompatible set of mechanical properties, even under a 30% strain condition (39). The NFC electronics facilitated image capture, and built-in sensors provided wireless, digital data on skin temperature (fig. S15 and movie S2).

After wirelessly collecting images, digital processing for assessment of color changes was achieved as shown in Fig. 4 (B to D). Reference color markers (true white and black) allowed white balancing to eliminate the dependence of the analysis on lighting conditions of practical relevance (daylight, shadow, and various light sources) (fig. S6). In particular, a white dot in the middle of the device and four black crosses distributed near the center established values for 100% and 0% in %RGB coordinates, respectively (Fig. 4B). The crosses further allowed rotations/translations of the images to facilitate accurate analysis of sweat rate and volume on the serpentine channel (fig. S7). After image correction, the digital color data (in %RGB format) were converted into analyte concentrations using calibration curves (Fig. 4D). We could reliably measure changes of 0.5 pH units and 0.2, 0.3, and 0.1 mM of chloride, lactate, and glucose concentrations, respectively, corresponding to a 1% change in the R channel of the RGB images. The calibration curve in Fig. 4C captures the pseudo-linearities associated with the serpentine shape of the channel. The angle of the filling front (the leading edge of the color change) in the serpentine channel defined the volume of sweat collected, thereby allowing calculation of total sweat loss and, with the time interval, total sweat rate.

Human testing of the skin-mounted sweat sensor

The first demonstration involved nine human subjects with devices mounted on two different body locations (lower back and volar forearm, Fig. 5B) and with two different harvesting areas (size of the opening in the adhesive shown in Fig. 5A) during intermediate-level activity on cycle ergometers under controlled temperature (38°C) and 50% relative humidity conditions. We compared the performance of the device in situ to conventional procedures that use absorbing pads applied onto the skin with subsequent weighing and laboratory-based analyses, such as spectrophotometry.

We quantified regional sweat rate normalized to unit area over the course of 1 hour (Fig. 5, C and D). Although the rates exhibited great variation among individual subjects, those measured on the lower back were typically ~2.3-fold greater than on the volar forearm, consistent with expectations from studies using conventional techniques (54). Rates determined using devices with large harvesting areas showed agreement with those obtained using absorbing pads (Fig. 5E). Furthermore, the devices accurately captured the volume and rate information continuously, without the need for removal. Notably, the y intercept in Fig. 5E corresponds to the limit of sweat measurement with the absorbing pad due to water evaporation (0.349 g/cm^2s of water evaporation at 38 °C, 50% relative humidity) during sample collection, highlighting one of its limitations. Devices with small harvesting areas yielded somewhat higher inferred rates than those with larger harvesting areas, perhaps due to alternations in perspiration behavior caused by the physical presence of the device (Fig. 5E) (55).

Concentrations of the markers chloride, glucose, lactate, and pH obtained by the colorimetric readouts demonstrated excellent agreement with conventional laboratory analysis of sweat collected from absorbing pads as shown in Fig. 5F. The glucose concentration in sweat from healthy subjects fell below the LOD for both image and laboratory analysis ($P < 0.05$ refers to differences in background noise only). Bivariate and multivariate statistical analyses, together with Pearson correlation heatmaps and Spearman rank-order statistics, quantified the correlations for all markers tested (fig. S16). The correlation between variations in marker analysis across individual subjects was only partially demonstrated because of the small sample size.

To examine the mechanical and fluidic integrity of the devices in a demanding exercise scenario, we assessed robustness in adhesion and fluidic collection and capture using devices on volunteers in a competitive long-distance outdoor bicycling race—El Tour de Tucson. Testing involved device placement on the lower back and the volar surface of the forearm of 12 volunteer riders (Fig. 6B). In all cases, the devices performed as anticipated, successfully collecting sweat with regional colorimetric change without patch detachment, even with substantial changes in temperature and humidity. Participants reported no sense of discomfort or limitation in body or arm movement during the cycling. Older subjects (ages

50 to 69 years) had greater rates of sweating in comparison to that of younger subjects (ages 10 to 29 years), and male subjects exhibited greater rates of sweating than females (Fig. 6E).

DISCUSSION

The epidermal microfluidic devices introduced here represent versatile platforms for evaluating athletic performance and monitoring health and disease status. The reported embodiments can detect sweat volume and rate, as well as several key markers including glucose, creatinine, lactate, chloride, and pH. Compared to previously described technologies for sweat analysis consisting of porous materials and fabrics or hydrogels as fluidic interfaces, our systems are unique in their use of fully integrated, soft microfluidics consisting of a network of functionalized channels and reservoirs for sweat capture, routing, and storage with spatially separated regions for analysis. By exploiting advanced concepts in microfluidic total analysis systems and lab-on-a-chip technologies and integrating skin-conformal electronics, our devices have the potential to provide further quantitative modes of use beyond opportunities afforded by the embodiments reported here or by other approaches. In addition to systematic investigations of the key engineering aspects and design parameters, initial studies demonstrated practical utility through tests on nine volunteers during moderate-intensity exercise in controlled conditions, with correlation of measured results to standard methods based on absorbent pads and laboratory chemical analyses. Evaluations on 12 cyclists during high-intensity physical exertion revealed real-word performance without loss of adhesion, leakage of fluids or other modes of failure, and without discomfort or irritation at the device/skin interface.

The soft mechanical properties, biocompatible constituent materials, digitally analyzable colorimetric responses, and overall careful optimization of structural, evaporative and fluidic properties are integral to the effectiveness of these devices and differentiate them from other sweat analysis technologies. Future opportunities could explore the use of these technologies for real-time, in situ sweat analysis and as storage vehicles for ex situ laboratory evaluation. In this latter context, it is important to note that we observed that the microfluidics structures described here can hold captured sweat for ~125 hours upon removal from the skin and sealing of the open channels (~75 hours without sealing) with negligible deterioration of colorimetric analysis. These possibilities, together with the development of on-board stretchable electronics for electrochemical biosensing, represent important directions of future research.

The limitations of the current devices are primarily in the range of chemical reagents that are available for accurate colorimetric analysis of markers at relevant ranges of concentration. Potential exists for extending colorimetric schemes to include enzymatic reactions or chromogens aimed at a broad range of possible applications for specific clinical diagnosis or for illicit drug use detection. However, the microfluidic channel/reservoir designs reported here cannot be easily designed to provide information on time-dependent changes in marker concentration detection. Advanced electronic or nonelectronic strategies for such temporal tracking of sweat chemistry are, therefore, of interest. An alternative approach is in microfluidic designs that enable time-dependent sampling of sweat into spatially distinct reservoirs for separate analysis. In all cases, digital image capture analysis represents a simple, ‘wireless’ means of quantitation. Direct electronic readout represents an additional possibility, where epidermal power supplies or wireless power transfer schemes could be useful. Further field studies are needed to demonstrate accuracy in realistic, demanding use scenarios.

In addition to their use in sweat monitoring, similar systems can be used as direct capture and storage vehicles for subsequent colorimetric or conventional laboratory-based analysis for various accumulated biofluids such as tears, saliva, or discharges from wounds, especially for small sample volume collection (<~50 μl). The same platforms can be combined with electronic or pharmacological means to actively initiate the release of sweat or extraction of other biofluids (for example, interstitial fluids). In both active and passive collection modes, the devices could be used in athletic and military training to gain insight into critical electrolyte loss, thereby guiding earlier supplementation before symptomatic cramping and “hitting the wall” points in time at which appropriate preventative treatment is no longer effective. In this scenario, and in others of interest, data accumulated over time from individual users could serve as the basis for the development of analytic approaches for interpreting trends in marker concentrations, with the potential to provide warning signs associated with physical activities that lead to abnormal responses. The intrinsically simple, low-cost nature of the devices may facilitate rapid, broad distribution for use in these contexts.

Materials and Methods

Study design

The objectives of indoor and outdoor human trial studies were to investigate feasibility of using these epidermal microfluidics devices in practical scenarios under controlled and uncontrolled environmental conditions and during moderate and vigorous exercise. Nine subjects were recruited through the Clinical Research Laboratory, LLC for indoor studies with anonymous collections of information including date of birth, gender, contraceptive status, weight, height, body mass index (BMI), blood pressure, and information from a simple survey of medical condition to ensure all subjects were healthy. The experimental conditions, including temperature, humidity, time course of application of device, and weight of absorbing Webril pads for sweat collection were all controlled and documented. Results obtained from image analysis methods (described in “Near-field communication and image processing for quantitative analysis” in Supplementary Materials) were compared with those from chemical laboratory analysis. For the outdoor study, 12 healthy subjects volunteered under eligibility requirements including enrollment and participation in El Tour de Tucson, a 104-km bike race. Age, height, and weight were recorded from subjects at the start of the race and used to calculate BMI and body surface area (BSA). Environmental conditions including temperature, humidity, and UV index were recorded every 2 and 3 hours from information provided by the National Weather Service. In both studies, sweat patches were placed on two different geographical body areas (volar arm and lower back) and image data were obtained by smartphone and digital single-lens reflex cameras. For full details, see Supplementary Materials.

Fabrication of epidermal microfluidic devices with integrated electronics for colorimetric sweat analysis

Standard soft lithographic techniques enabled fabrication of epidermal microfluidic devices (56). Briefly, casting and curing PDMS against lithographically prepared molds yielded solid elastomers with features of relief on their surfaces. Bonding separate pieces of PDMS formed in this manner defined sealed microfluidic channels and containment reservoirs. Mechanical punches created openings to define the inlets for sweat collection. A separate, double-sided thin adhesive layer with matching holes bonded to the bottom surface of the device on one side and to the skin on the other. As an option, separately fabricated thin electronic systems with open architectures were mounted on the top surface. For colorimetric analysis, the chromogenic reagents for detecting glucose (a mixture of glucose oxidase, horseradish peroxidase, trehalose, and potassium iodide in sodium citrate buffer solution), lactate (D-Lactase Assay Kit; Sigma-Aldrich), chloride [chloride detection reagent (Chloride Assay Kit; Sigma-Aldrich) titrated with $Hg(SCN)_2$], and pH [universal pH indicator solution (Ricca Chemical Company)] were spotted onto filter paper and inserted into containment reservoirs. Cobalt chloride dissolved in pHEMA hydrogel served as a sensor of water in the serpentine channels. Complete fabrication and colorimetric analysis details are provided in the Supplementary Materials.

Statistical analysis

Data are presented with average values and SD unless noted in the figure caption. Pearson and Spearman correlation analyses were conducted on the patch and laboratory results (fig. S16). The matrix of bivariate correlations in analyte concentrations between the patch and lab analysis are displayed using a heat map representation. Blue and red denote negative and positive correlations, respectively. Bivariate correlations are described using Spearman rank-order statistics. Analyses were performed using SAS and JMP statistical software.

Supplementary Material

Refer to Web version on PubMed Central for supplementary material.

Acknowledgments

Funding: This work was supported by L'Oréal and the Frederick Seitz Materials Research Laboratory at the University of Illinois at Urbana-Champaign. J.K. and U.P. acknowledge the support from Global Research Laboratory Program (K20704000003TA050000310) through the National Research Foundation of Korea funded by the Ministry of Science. Y.H. acknowledges NIH R01EB019337.

References

1. Kim DH, Lu N, Ma R, Kim YS, Kim RH, Wang S, Wu J, Won SM, Tao H, Islam A. Epidermal electronics. Science. 2011; 333:838–843. [PubMed: 21836009]
2. Rogers JA. Electronics for the human body. JAMA. 2015; 313:561–562. [PubMed: 25668256]
3. Kaltenbrunner M, Sekitani T, Reeder J, Yokota T, Kuribara K, Tokuhara T, Drack M, Schwödiauer R, Graz I, Bauer-Gogonea S. An ultra-lightweight design for imperceptible plastic electronics. Nature. 2013; 499:458–463. [PubMed: 23887430]

4. Lipomi DJ, Vosgueritchian M, Tee BC, Hellstrom SL, Lee JA, Fox CH, Bao Z. Skin-like pressure and strain sensors based on transparent elastic films of carbon nanotubes. Nature Nanotech. 2011; 6:788–792.
5. Takei K, Takahashi T, Ho JC, Ko H, Gillies AG, Leu PW, Fearing RS, Javey A. Nanowire active-matrix circuitry for low-voltage macroscale artificial skin. Nature Mater. 2010; 9:821–826. [PubMed: 20835235]
6. Kang D, Pikhitsa PV, Choi YW, Lee C, Shin SS, Piao L, Park B, Suh K-Y, Kim T-i, Choi M. Ultrasensitive mechanical crack-based sensor inspired by the spider sensory system. Nature. 2014; 516:222–226. [PubMed: 25503234]
7. Dagdeviren C, Shi Y, Joe P, Ghaffari R, Balooch G, Usgaonkar K, Gur O, Tran PL, Crosby JR, Meyer M. Conformal piezoelectric systems for clinical and experimental characterization of soft tissue biomechanics. Nature Mater. 2015; 14:728–736. [PubMed: 25985458]
8. Webb RC, Bonifas AP, Behnaz A, Zhang Y, Yu KJ, Cheng H, Shi M, Bian Z, Liu Z, Kim YS. Ultrathin conformal devices for precise and continuous thermal characterization of human skin. Nature Mater. 2013; 12:938–944. [PubMed: 24037122]
9. Viventi J, Kim DH, Vigeland L, Frechette ES, Blanco JA, Kim YS, Avrin AE, Tiruvadi VR, Hwang SW, Vanleer AC. Flexible, foldable, actively multiplexed, high-density electrode array for mapping brain activity in vivo. Nat Neurosci. 2011; 14:1599–1605. [PubMed: 22081157]
10. Jeong JW, Yeo WH, Akhtar A, Norton JJS, Kwack YJ, Li S, Jung SY, Su Y, Lee W, Xia J, Cheng H, Huang Y, Choi WS, Bretl T, Rogers JA. Materials and optimized designs for human-machine interfaces via epidermal electronics. Advanced Materials. 2013; 25:6839–6846. [PubMed: 24327417]
11. Matzeu G, Florea L, Diamond D. Advances in wearable chemical sensor design for monitoring biological fluids. Sens Actuators B Chem. 2015; 211:403–418.
12. Corrie S, Coffey J, Islam J, Markey K, Kendall M. Blood, sweat, and tears: developing clinically relevant protein biosensors for integrated body fluid analysis. Analyst. 2015; 140:4350–4364. [PubMed: 25909342]
13. Sonner Z, Wilder E, Heikenfeld J, Kasting G, Beyette F, Swaile D, Sherman F, Joyce J, Hagen J, Kelley-Loughnane N, Naik R. The microfluidics of the eccrine sweat gland, including biomarker partitioning, transport, and biosensing implications. Biomicrofluidics. 2015; 9:031301. [PubMed: 26045728]
14. Gao W, Emaminejad S, Nyein HYY, Challa S, Chen K, Peck A, Fahad HM, Ota H, Shiraki H, Kiriya D, Lien DH, Brooks GA, Davis RW, Javey A. Fully integrated wearable sensor arrays for multiplexed in situ perspiration analysis. Nature. 2016; 529:509–514. [PubMed: 26819044]
15. Heikenfeld J. Non-invasive Analyte Access and Sensing through Eccrine Sweat: Challenges and Outlook circa 2016. Electroanalysis. 2016; 28:1242–1249.
16. Salvo P, Di Francesco F, Costanzo D, Ferrari C, Trivella MG, De Rossi D. A wearable sensor for measuring sweat rate. IEEE Sensors J. 2010; 10:1557–1558.
17. Jadoon S, Karim S, Akram MR, Kalsoom Khan A, Zia MA, Siddiqi AR, Murtaza G. Recent developments in sweat analysis and its applications. 2015; 2015:7.
18. Shirreffs SM, Maughan RJ. Whole body sweat collection in humans: an improved method with preliminary data on electrolyte content. J Appl Physiol. 1997; 82:336–341. [PubMed: 9029235]
19. LeGrys, VA., Applequist, R., Farrell, P., Hickstein, R., Lo, SF., Passarell, R., Rheinheimer, DW., Rosenstein, BJ., Vaks, JE. Sweat testing: Sample collection and quantitative Analysis, approved guideline [Document C34–A3]. National Committee for Clinical Laboratory Standards; Wayne, PA: 2000.
20. Coyle S, Lau KT, Moyna N, O’Gorman D, Diamond D, Di Francesco F, Costanzo D, Salvo P, Trivella MG, De Rossi DE, Taccini N, Paradiso R, Porchet JA, Ridolfi A, Luprano J, Chuzel C, Lanier T, Revol-Cavalier F, Schoumacker S, Mourier V, Chartier I, Convert R, De-Moncuit H, Bini C. BIOTEX--biosensing textiles for personalised healthcare management. IEEE Trans Inf Technol Biomed. 2010; 14:364–370. [PubMed: 20064761]
21. Jia W, Bandodkar AJ, Valdés-Ramírez G, Windmiller JR, Yang Z, Ramírez J, Chan G, Wang J. Electrochemical tattoo biosensors for real-time noninvasive lactate monitoring in human perspiration. Analytical Chemistry. 2013; 85:6553–6560. [PubMed: 23815621]

22. Guinovart T, Bandodkar AJ, Windmiller JR, Andrade FJ, Wang J. A potentiometric tattoo sensor for monitoring ammonium in sweat. Analyst. 2013; 138:7031–7038. [PubMed: 24098883]
23. Bandodkar AJ, Molinnus D, Mirza O, Guinovart T, Windmiller JR, Valdes-Ramirez G, Andrade FJ, Schoning MJ, Wang J. Epidermal tattoo potentiometric sodium sensors with wireless signal transduction for continuous non-invasive sweat monitoring. Biosens Bioelectron. 2014; 54:603–609. [PubMed: 24333582]
24. Curto VF, Fay C, Coyle S, Byrne R, O'Toole C, Barry C, Hughes S, Moyna N, Diamond D, Benito-Lopez F. Real-time sweat pH monitoring based on a wearable chemical barcode micro-fluidic platform incorporating ionic liquids. Sensor Atuat B-Chem. 2012; 171–172:1327–1334.
25. Oncescu V, O'Dell D, Erickson D. Smartphone based health accessory for colorimetric detection of biomarkers in sweat and saliva. Lab Chip. 2013; 13:3232–3238. [PubMed: 23784453]
26. Shen L, Hagen JA, Papautsky I. Point-of-care colorimetric detection with a smartphone. Lab on a Chip. 2012; 12:4240–4243. [PubMed: 22996728]
27. Rose D, Ratterman M, Griffin D, Hou L, Kelley-Loughnane N, Naik R, Hagen J, Papautsky I, Heikenfeld J. Adhesive RFID sensor patch for monitoring of sweat electrolytes. IEEE Trans Biomed Eng. 2014; 62:1457–1465. [PubMed: 25398174]
28. Huang X, Liu Y, Chen K, Shin W-J, Lu C-J, Kong G-W, Patnaik D, Lee S-H, Cortes JF, Rogers JA. Stretchable, wireless sensors and functional substrates for epidermal characterization of sweat. Small. 2014; 10:3083–3090. [PubMed: 24706477]
29. Gao L, Zhang Y, Malyarchuk V, Jia L, Jang K-I, Chad Webb R, Fu H, Shi Y, Zhou G, Shi L, Shah D, Huang X, Xu B, Yu C, Huang Y, Rogers JA. Epidermal photonic devices for quantitative imaging of temperature and thermal transport characteristics of the skin. Nat Commun. 2014; 5
30. Kim, T-i, McCall, JG., Jung, YH., Huang, X., Siuda, ER., Li, Y., Song, J., Song, YM., Pao, HA., Kim, R-H. Injectable, cellular-scale optoelectronics with applications for wireless optogenetics. Science. 2013; 340:211–216. [PubMed: 23580530]
31. Jeong J-W, McCall Jordan G, Shin G, Zhang Y, Al-Hasani R, Kim M, Li S, Sim Joo Y, Jang K-I, Shi Y, Hong Daniel Y, Liu Y, Schmitz Gavin P, Xia L, He Z, Gamble P, Ray Wilson Z, Huang Y, Bruchas Michael R, Rogers John A. Wireless optofluidic systems for programmable in vivo pharmacology and optogenetics. Cell. 2015; 162:662–674. [PubMed: 26189679]
32. Sato K, Sato F. Individual variations in structure and function of human eccrine sweat gland. Am J Physiol Regul Integr Comp Physiol. 1983; 245:R203–R208.
33. Klode J, Schöttler L, Stoffels I, Körber A, Schadendorf D, Dissemond J. Investigation of adhesion of modern wound dressings: a comparative analysis of 56 different wound dressings. Journal of the European Academy of Dermatology and Venereology. 2011; 25:933–939. [PubMed: 21062365]
34. Wilke K, Martin A, Terstegen L, Biel SS. A short history of sweat gland biology. Int J Cosmet Sci. 2007; 29:169–179. [PubMed: 18489347]
35. Lee JN, Park C, Whitesides GM. Solvent compatibility of poly (dimethylsiloxane)-based microfluidic devices. Anal Chem. 2003; 75:6544–6554. [PubMed: 14640726]
36. Kim DH, Ghaffari R, Lu N, Rogers JA. Flexible and Stretchable Electronics for Biointegrated Devices. Annual Review of Biomedical Engineering. 2012; 14:113–128.
37. Lee CH, Ma Y, Jang KI, Banks A, Pan T, Feng X, Kim JS, Kang D, Raj MS, McGrane BL, Morey B, Wang X, Ghaffari R, Huang Y, Rogers JA. Soft core/shell packages for stretchable electronics. Adv Funct Mater. 2015; 25:3698–3704.
38. Liang X, Boppart S. Biomechanical properties of in vivo human skin from dynamic optical coherence elastography. IEEE Trans Biomed Eng. 2010; 57:953–959. [PubMed: 19822464]
39. Kim J, Banks A, Cheng HY, Xie ZQ, Xu S, Jang KI, Lee JW, Liu ZJ, Gutruf P, Huang X, Wei PH, Liu F, Li K, Dalal M, Ghaffari R, Feng X, Huang YG, Gupta S, Paik U, Rogers JA. Epidermal electronics with advanced capabilities in near-field communication. Small. 2015; 11:906–912. [PubMed: 25367846]
40. Huang YY, Zhou W, Hsia KJ, Menard E, Park JU, Rogers JA, Alleyne AG. Stamp collapse in soft lithography. Langmuir. 2005; 21:8058–8068. [PubMed: 16089420]
41. Pang C, Lee GY, Kim TI, Kim SM, Kim HN, Ahn SH, Suh KY. A flexible and highly sensitive strain-gauge sensor using reversible interlocking of nanofibres. Nature Mater. 2012; 11:795–801. [PubMed: 22842511]

42. Hou L, Hagen J, Wang X, Papautsky I, Naik R, Kelley-Loughnane N, Heikenfeld J. Artificial microfluidic skin for in vitro perspiration simulation and testing. Lab on a Chip. 2013; 13:1868–1875. [PubMed: 23576120]
43. Taylor NA, Machado-Moreira CA. Regional variations in transepidermal water loss, eccrine sweat gland density, sweat secretion rates and electrolyte composition in resting and exercising humans. Extrem Physiol Med. 2013; 2:1–30. [PubMed: 23849512]
44. Polliack A, Taylor R, Bader D. Sweat analysis following pressure ischaemia in a group of debilitated subjects. JRRD. 1997; 34:303–308.
45. Biagi S, Ghimenti S, Onor M, Bramanti E. Simultaneous determination of lactate and pyruvate in human sweat using reversed-phase high-performance liquid chromatography: a noninvasive approach. Biomed Chromatogr. 2012; 26:1408–1415. [PubMed: 22311625]
46. Alvear-Ordenes I, García-López D, De Paz JA, González-Gallego J. Sweat lactate, ammonia, and urea in rugby players. Int J Sports Med. 2005; 26:632–637. [PubMed: 16158367]
47. Lamont LS. Sweat lactate secretion during exercise in relation to women's aerobic capacity. Journal of Applied Physiology. 1987; 62:194–198. [PubMed: 3558180]
48. Martinez AW, Phillips ST, Butte MJ, Whitesides GM. Patterned paper as a platform for inexpensive, low-volume, portable bioassays. Angew Chem Int Edit. 2007; 46:1318–1320.
49. Martinez AW, Phillips ST, Carrilho E, Thomas SW, Sindi H, Whitesides GM. Simple telemedicine for developing regions: camera phones and paper-based microfluidic devices for real-time, off-site diagnosis. Anal Chem. 2008; 80:3699–3707. [PubMed: 18407617]
50. Boysen TC, Yanagawa S, Sato F, Sato K. A modified anaerobic method of sweat collection. Journal of Applied Physiology. 1984; 56:1302–1307. [PubMed: 6327585]
51. Wei H, Wang E. Fe3O4 Magnetic Nanoparticles as Peroxidase Mimetics and Their Applications in H2O2 and Glucose Detection. Analytical Chemistry. 2008; 80:2250–2254. [PubMed: 18290671]
52. Song Y, Qu K, Zhao C, Ren J, Qu X. Graphene oxide: intrinsic peroxidase catalytic activity and its application to glucose detection. Advanced Materials. 2010; 22:2206–2210. [PubMed: 20564257]
53. Crocker H, Shephard M, White G. Evaluation of an enzymatic method for determining creatinine in plasma. Journal of clinical pathology. 1988; 41:576–581. [PubMed: 3384988]
54. Smith CJ, Havenith G. Body mapping of sweating patterns in male athletes in mild exercise-induced hyperthermia. Eur J Appl Physiol. 2011; 111:1391–1404. [PubMed: 21153660]
55. Licht PB, Pilegaard HK. Severity of compensatory sweating after thoracoscopic sympathectomy. Ann Thorac Surg. 2004; 78:427–431. [PubMed: 15276490]
56. Fainman, Y., Lee, L., Psaltis, D., Yang, C. Optofluidics: Fundamentals, Devices, and Applications Ch.2. McGraw-Hill Education; New York, NY: 2009.
57. Ventsel, E., Krauthammer, T. Thin Plates and Shells: Theory: Analysis, and Applications. CRC Press; 2001.
58. White, FM. Fluid Mechanics. 7. McGraw-Hill Higher Education; 2010.

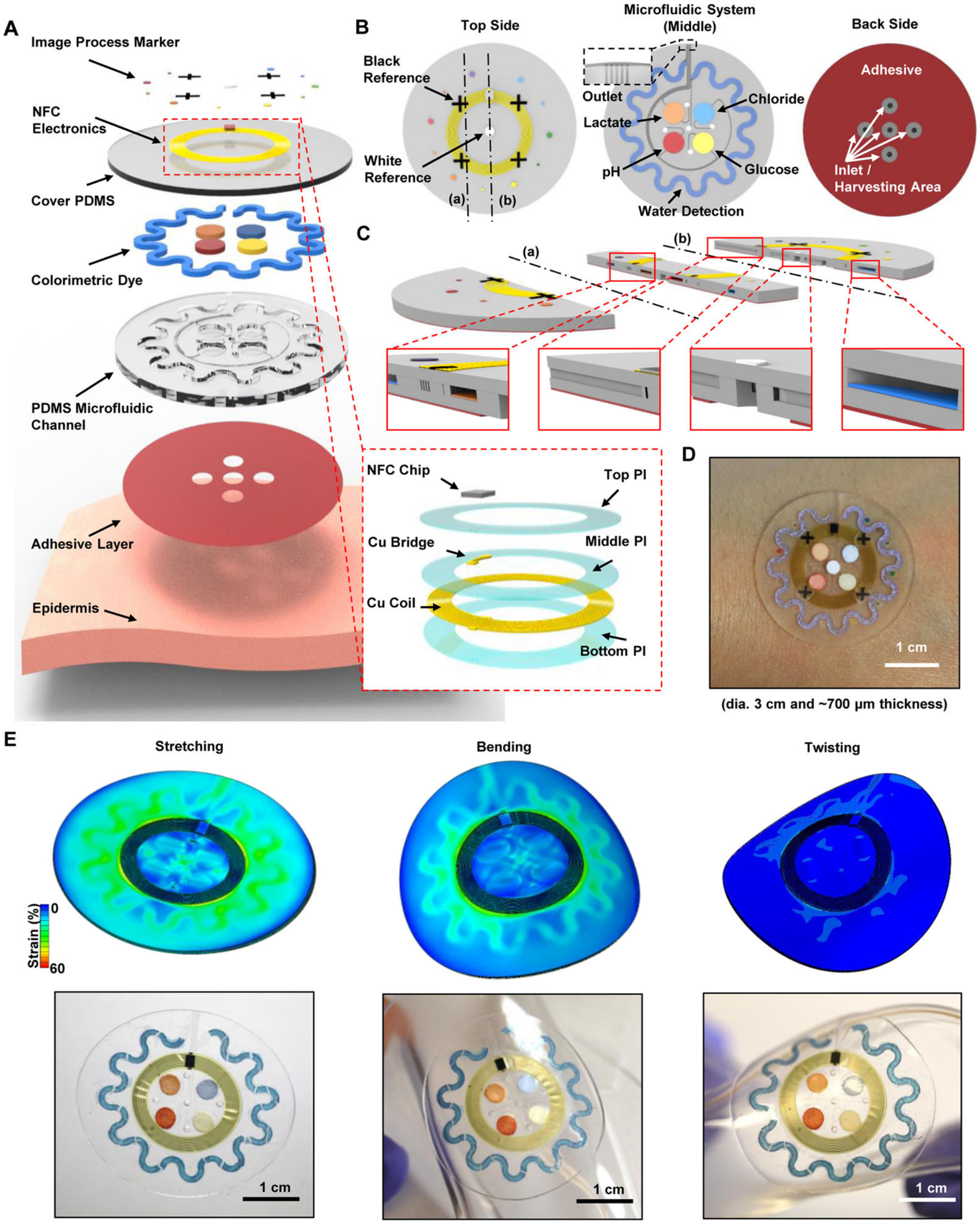

Fig. 1. Schematic illustrations, optical images, and theoretical stress modeling of an epidermal microfluidic biosensor integrated with flexible electronics for sweat monitoring

(A) Schematic illustration of an epidermal microfluidic sweat monitoring device and an enlarged image of the integrated near-field communication (NFC) system (inset). **(B)** Illustration of the top, middle, and back sides of the device. The reference color (white and black) markers are on the top side, along with the NFC electronics. The microfluidic channels with colorimetric assay reagents (water, lactate, chloride, glucose, and pH) are in the middle. The bottom side consists of a uniform layer of adhesive bonded to the bottom surfaces of the PDMS-enclosed microchannels, with openings that define sweat access and inlets that connect to these channels. **(C)** Cross-sectional diagrams of the cuts defined by the dashed lines (a) and (b) shown in the top side illustration in (B). (**D**) Optical image of a fabricated device mounted on the forearm. **(E)** FEA results of stress distribution associated with the devices on phantom skin (PDMS) and respective optical images under various mechanical distortions: stretching at 30 % strain, bending with 5 cm radius, and twisting.

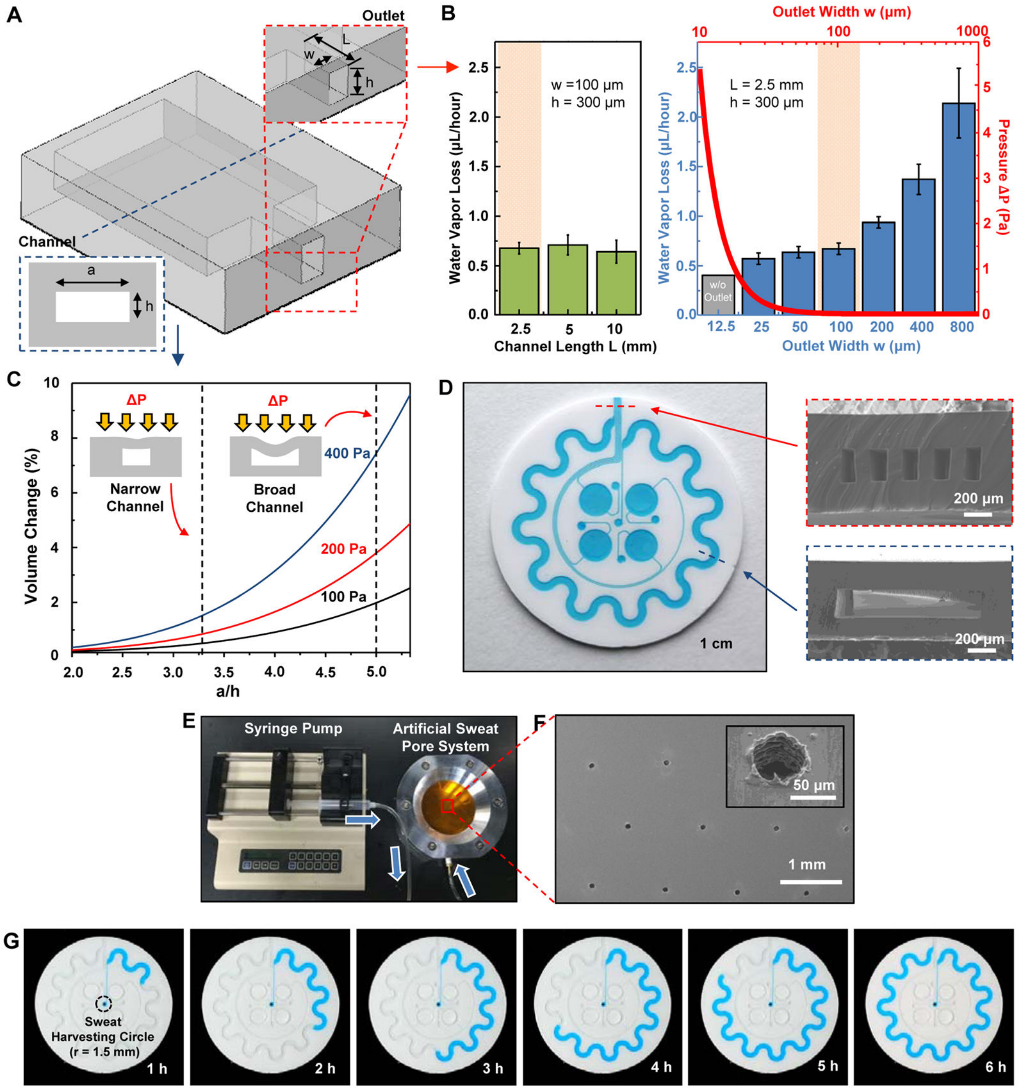

Fig. 2. Analysis of key design features and demonstration of epidermal microfluidic devices

(A) Sketch of the channel geometry for numerical calculation. The blue and red dashed boxes highlight the dimensions of the serpentine and outlet channels, respectively. **(B)** Experimentally determined water vapor loss from a microfluidic channel as a function of width (w) and length (L) of the outlet channel with a fixed height of 300 μm. Inner pressure variation as a function of the outlet channel width was also determined from the model (red line). The orange shading highlights the optimal channel geometry. Data are presented as the average value, and error bars represent SD (n=3). (**C)** Model prediction of the change in volume of the serpentine channel as a function of AR [ratio of width *a* to height *h* of the serpentine channel in (A), blue dashed box] under various pressures (ΔP = 100, 200 and 400 Pa). ΔP represents pressure difference between the inside and outside of the serpentine channel. Dotted vertical lines show two representative ARs (10:3 and 5:1). **(D)** Picture of a fabricated epidermal microfluidic structure corresponding to the theoretical results and cross-sectional scanning electron microscope (SEM) images of the outlet (red dashed box) and serpentine (blue dashed box) channels. **(E)** Experimental setup of artificial sweat pore system. **(F)** SEM images of the polyimide (PI) membrane mimicking human sweat glands. **(G)** Demonstration of hydrodynamic fluid flow through the microfluidic device using the artificial sweat pore system at the rate of 5.5 μl/hour.

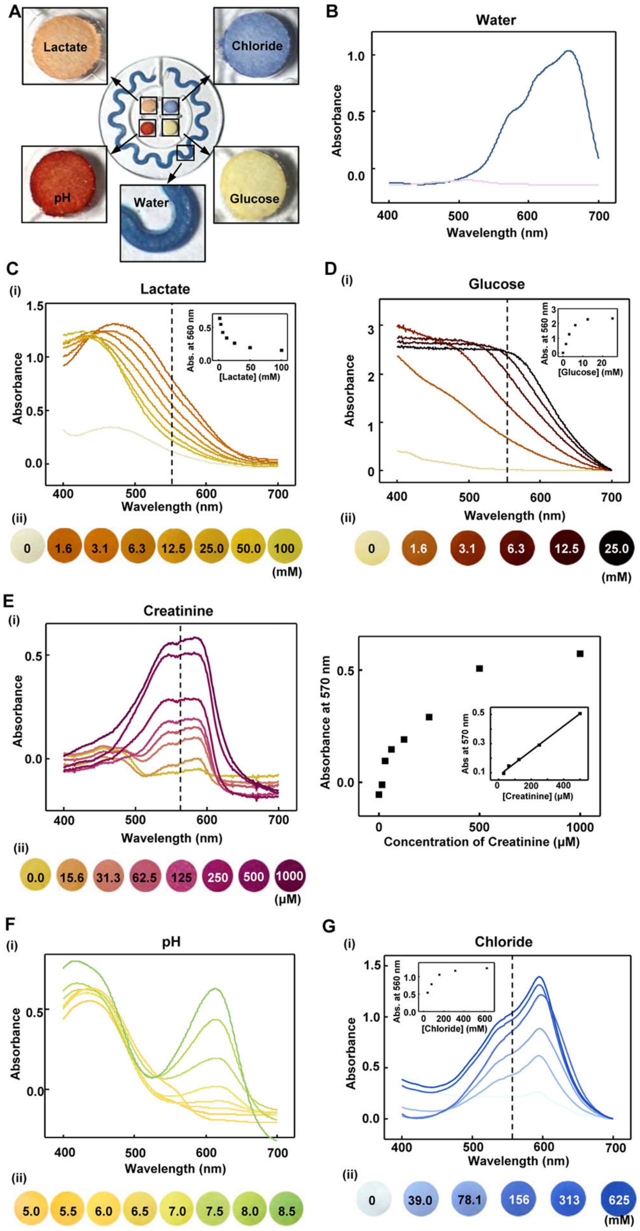

Fig. 3. Quantitative colorimetric analysis of markers in sweat

(A) Colorimetric detection reservoirs that enable determination of **(B)** total water (sweat) loss and concentrations of **(C)** lactate, **(D)** glucose, **(E)** creatinine, **(F)** pH, and **(G)** chloride ions in sweat. (B to G) Corresponding quantitative analysis conducted by (i) ultraviolet (UV)-visible spectroscopy and (ii) optical images as a function of analyte concentration. The presented color for (i) each spectrum corresponds to (ii) the color exhibited at the detection reservoir in the device. The insets in the spectra provide calibration curves for each of the analytes. The inset in **(E)** shows the response over a reduced range of concentrations.

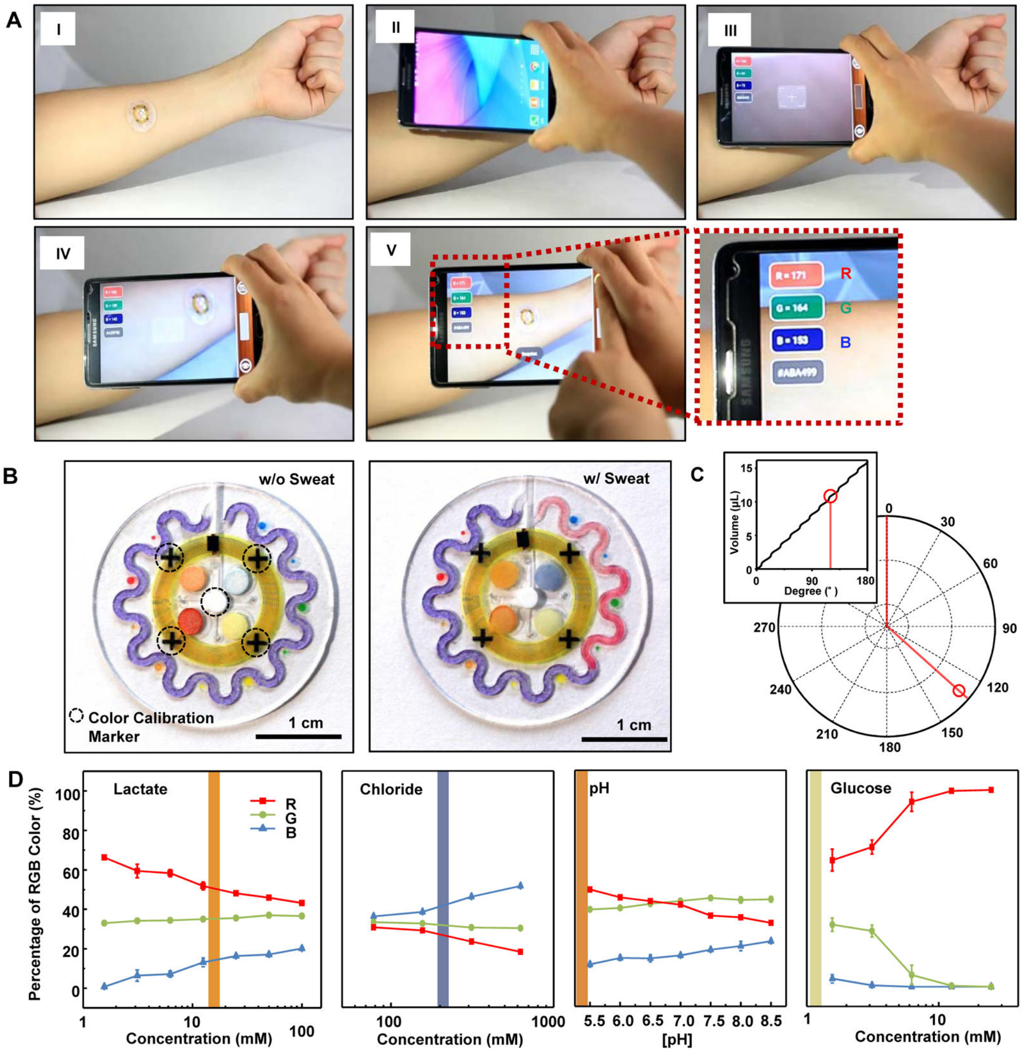

Fig. 4. NFC interface to a smartphone and image processing approaches

(A) Pictures demonstrating NFC between a sweat monitoring device and a smartphone to launch software for image capture and analysis. **(B)** Images of the epidermal microfluidic biosensor (left) before and (right) after injecting artificial sweat. **(C)** Location tracking of sweat accumulation with polar coordinates and their relationship to total captured volume of sweat (inset). **(D)** Standard calibration curves between normalized %RGB value and concentration of markers for quantitative analysis (n=3, error bars represent the SD). Each vertical colored bar represents the marker concentration determined from the corresponding reservoirs in the right image of **(B)** as an example.

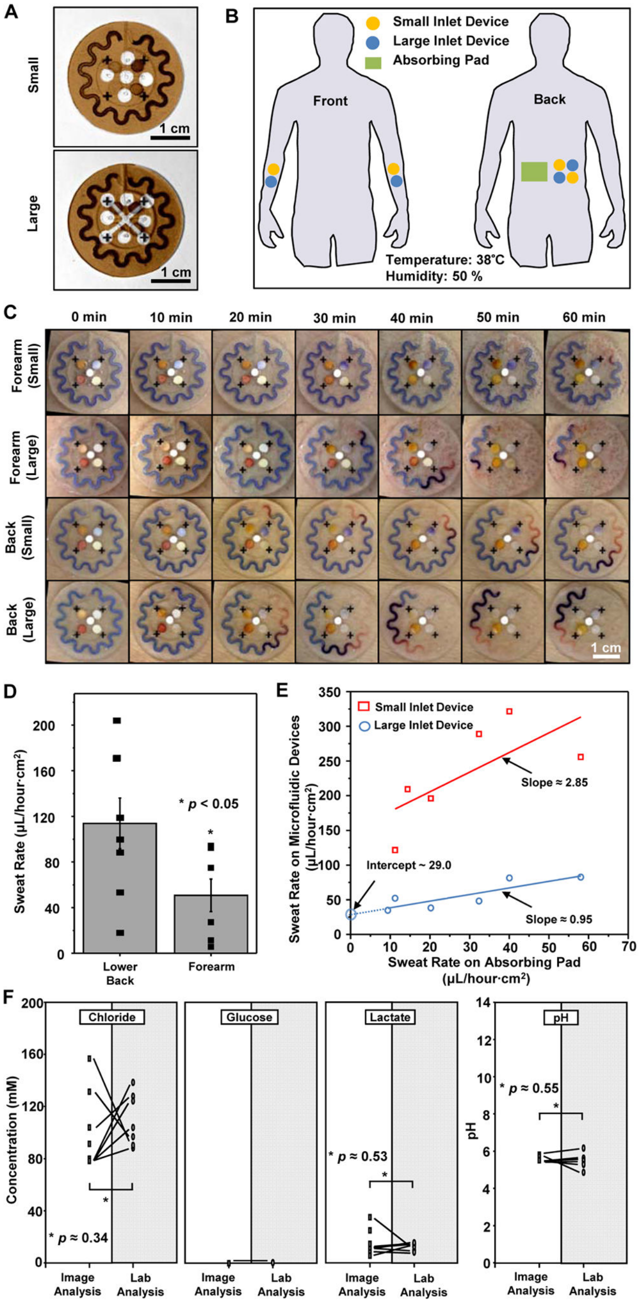

Fig. 5. Human trials of sweat monitoring devices in a temperature- and humidity-controlled room (35°C at 50% relative humidity)

(A) Images of two device designs used for the studies. The brown color corresponds to the adhesive layer on the back sides of the devices, with small and large harvesting areas (inlets). Absorbing pads served as reference controls. **(B)** Illustration indicating locations of sweat patches on the subjects (volar forearm and lower back). **(C)** Images of two different types of sweat patches (small and large harvesting areas) applied to the lower back and volar forearm collected at various times during the study. **(D)** Sweat rate determined at the lower back and volar forearm. Bars represent mean of n=8; error bars represent SD. $*P < 0.05$, two-tailed *t* test. **(E)** Correlation of sweat rate between the epidermal microfluidic devices and the reference-absorbing pads (n=7). **(F)** Marker concentrations in sweat obtained by image processing of data from the device (unshaded) versus laboratory-based analysis of sweat collected from absorbing pads (shaded) (n=7). $^{*}P < 0.05$, two-tailed *t* test.

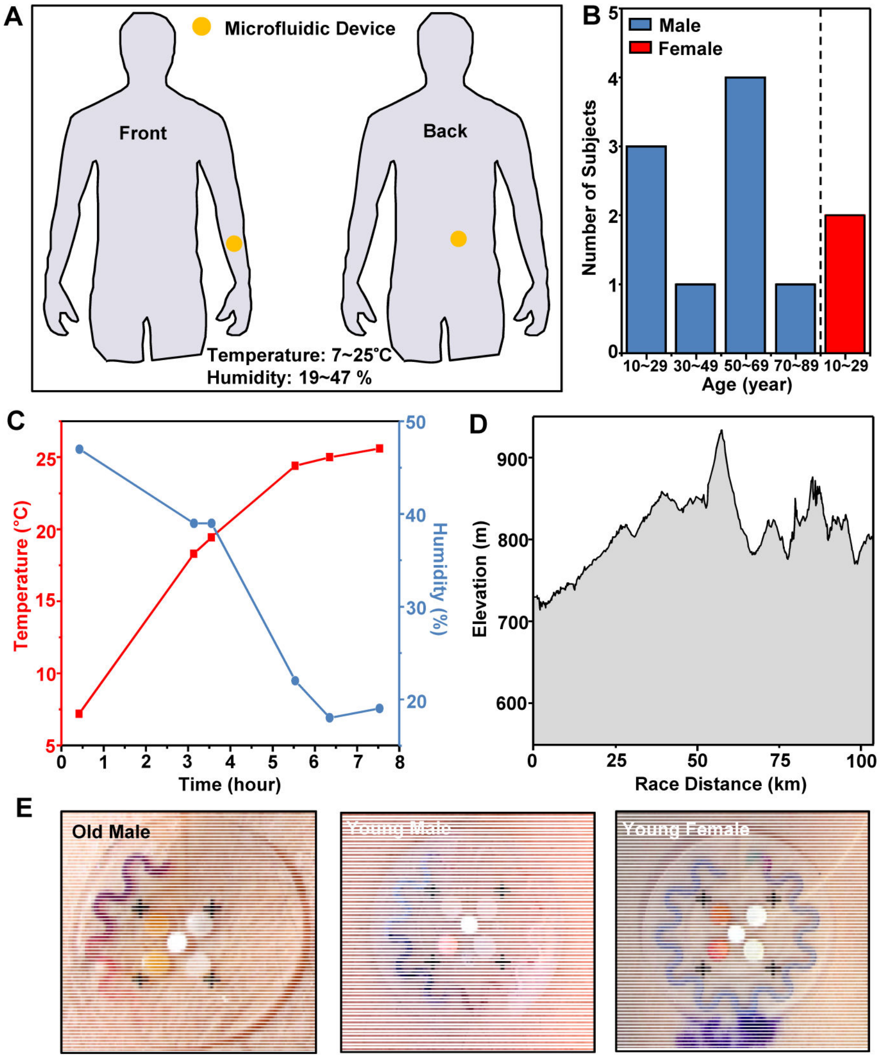

Fig. 6. Human trials of sweat monitoring devices on cyclists competed in an outdoor race

(A) Illustration of locations of devices on the cycling subjects (volar forearm and lower back). **(B)** Histogram of the age distribution of the subjects. **(C)** Temperature and humidity during the race. **(D)** Elevation profile of the course. **(E)** Devices on the volar forearms of several subjects, imaged after ~84 km of cycling (that is, middle point of total race). (The purple ink in the lower part of the image on the right is from a marking formed on the skin using a pen, prior to application of the device.)